# Attribution of Gamma-ray Background Collected by a Mobile Detector System to its Surroundings using Panoramic Video

Mark S. Bandstra[a,*], Brian J. Quiter[a], Joseph C. Curtis[a], Kyle J. Bilton[b], Tenzing H. Y. Joshi[a], Ross Meyer[a], Victor Negut[a], Kai Vetter[a,b], Daniel E. Archer[c], Donald E. Hornback[c,d], Douglas E. Peplow[c], Catherine E. Romano[c], Mathew W. Swinney[c], Thomas L. McCullough[e], M. S. Lance McLean[e]

[a] *Nuclear Science Division, Lawrence Berkeley National Laboratory, Berkeley, California*
[b] *Department of Nuclear Engineering, University of California Berkeley, California*
[c] *Oak Ridge National Laboratory, Oak Ridge, TN 37831*
[d] *NNSA/DNN R&D*
[e] *Remote Sensing Laboratory*

**Abstract**

Mobile radiation detector systems are important tools for detecting radiological and nuclear sources outside of regulatory control, but due to their mobility, they are subject to complex and varying backgrounds in most realistic operational scenarios. Recent work has found correlations between non-radiological contextual information and gamma-ray spectral features that can be used to decrease false alarm rates, however a more complete understanding of background source terms has been elusive. A measurement campaign developed a full radiological characterization of a controlled facility that roughly corresponded to two city blocks. As part of the campaign, the Radiological Multi-sensor Analysis Platform (RadMAP) collected extensive multi-sensor data. In this work, RadMAP's panoramic video data were used to visually identify several different materials and quantify the detector response to each material. A linear model was fit between the material responses and radiological features, and the results demonstrate reasonable agreement with ground truth flux measurements

*Corresponding author
*Email address:* msbandstra@lbl.gov (Mark S. Bandstra)

for each material. This paper will describe the data collection, processing, and analysis of the gamma-ray and video data from RadMAP. The paper will conclude with perspectives on the applicability of such a method to less controlled environments both with respect to achieving better understanding the sources of variability of background radiation in urban environments and whether such methods could be leveraged in operational scenarios.

*Keywords:* Gamma-ray detection, Background radiation, Data fusion, Homeland security

---

## 1. Introduction

Vehicle-borne radiological detector systems are becoming increasingly important tools for radiological and nuclear security because they can carry large ($\sim 1$ m$^2$) gamma-ray and neutron detectors and are thus more capable than smaller detectors of detecting weak sources [1–3]. However, larger detectors also collect more background events and are more sensitive to background fluctuations [4, 5]. Recent approaches have used multiple contextual (non-radiological) sensors to obtain data about the environment to find correlations between contextual and radiological features [6, 7]. However no system has yet shown the ability to completely attribute all of the measured background to the environment around the system. Such background "inversion," if possible, could allow a detector system to become less prone to alarms due to benign anomalies, which would result in improved sensitivity to threat sources in a search scenario. Inversion would also enable physics modeling of scenarios based on volumes of real-world data previously impractical to obtain.

The RadMAP system was developed as a testbed to explore correlations between radiological and contextual data [8]. RadMAP combines large volume gamma-ray and neutron detectors with contextual sensors such as panoramic video, LiDAR, and hyperspectral imagery. This paper describes measurements conducted with the RadMAP system in the Military Operations in Urban Terrain (MOUT) facility at the Fort Indiantown Gap (FTIG) National Guard

training facility that were part of the Multi-agency Urban Search Experiment (MUSE) in 2016 [9, 10]. MUSE seeks to thoroughly model and benchmark urban radiological environments, and as part of the effort at the FTIG MOUT facility, a thorough set of *in situ* ground truth measurements were taken with HPGe detectors [11]. The capabilities of RadMAP, combined with the site ground truth measurements, makes the FTIG MOUT dataset ripe for background inversion analysis.

The background inversion analysis presented herein is based on three streams of data generated by RadMAP: the NaI(Tl) gamma-ray detector array, the two Point Grey Ladybug3 panoramic video systems, and the NovAtel inertial navigation system (INS). The reader is referred to [8] for more detail on the specific systems used. Combining these three streams of data, we demonstrate correlations between the fraction of field of view subtended by visible objects and the radiological data generated by the on-board NaI(Tl) array.

## 2. Methodology

We assume a linear model that attributes detected gamma rays to pixels subtending the angular space surrounding the detector system. This model neglects air attenuation and second-order effects such as skyshine and scatter between objects in the environment. A full 3-D model of the environment would enable consideration of these effects, but they are neglected here.

All $4\pi$ steradians of solid angle surrounding the detector system are divided into small elements. Visual panoramic images are used to label all elements by material class, and a simulated detector model is used to estimate the response. Corrections to the response are applied to account for the placement of the panoramic video cameras relative to the detector system. Thereafter the measured spectral features are fit to a linear combination of the image-derived responses, where a constant activity for each material class is assumed. The resulting activities are compared to the gamma-ray emission source terms based on the ground truth measurements in Section 3.3.

### 2.1. Linear emission model

For a surface element $j$ of area $a_j$ with activity per area $\alpha_j$ emitting into $2\pi$ steradians, the flux (photons/second/area) at a distance $r_{ij}$ and angle from surface normal $\theta_{ij}$ is

$$\alpha_j \frac{a_j \cos\theta_{ij}}{2\pi r_{ij}^2}. \tag{1}$$

Here and hereafter, a far-field approximation is assumed. For a detector at position $i$ that has an effective area (product of detector efficiency and geometric area) $A_{ij}$ in the direction of surface $j$, the measured photons $y_{ij}$ for a dwell time $\Delta t_i$ can be approximated by

$$\begin{aligned} y_{ij} &\approx \alpha_j \frac{a_j \cos\theta_{ij}}{2\pi r_{ij}^2} A_{ij} \Delta t_i & (2) \\ &\approx \alpha_j \frac{\Delta\Omega_{ij}}{2\pi} A_{ij} \Delta t_i, & (3) \end{aligned}$$

where $\Delta\Omega_{ij} \equiv a_j \cos\theta_{ij}/r_{ij}^2$ is the solid angle of surface $j$ as seen by the detector at position $i$. Assuming the environment around the detector has been completely divided into surface elements indexed by $j$, the total number of photons measured at position $i$ is

$$y_i \approx \Delta t_i \sum_j A_{ij} \frac{\Delta\Omega_{ij}}{2\pi} \alpha_j. \tag{4}$$

This sum becomes

$$\begin{aligned} y_i &\approx \Delta t_i \sum_C \alpha_C \sum_{j\in C} \frac{\Delta\Omega_{ij}}{2\pi} A_{ij} & (5) \\ &\equiv \Delta t_i \sum_C R_{iC} \alpha_C & (6) \end{aligned}$$

by assuming surface elements are grouped into classes $C$ of equal surface flux $\alpha_C$ based on visual information. The quantity

$$R_{iC} \equiv \sum_{j\in C} \frac{\Delta\Omega_{ij}}{2\pi} A_{ij} \tag{7}$$

is referred to as the response for class $C$ at detector position $i$.

### 2.2. Dataset preparation

A period of continuous motion of the RadMAP vehicle from 10:37:28 to 11:33:18 EDT on 1 September 2016 was used in the analysis. During this period, the vehicle traveled in multiple laps around the entire MOUT facility. The typical vehicle speeds during the dataset were $2 - 8$ m/s. Although the panoramic cameras on RadMAP were triggered at a rate of 15 Hz, images were downsampled to a rate of 3 Hz in order to align with binnings of the gamma-ray data that result in relative statistical uncertainties of $\lesssim 2\%$ instead of $\sim 4\%$. There are a total of 10,047 images used during the 3,350 s dataset, and the full resolution of each image was 5400×2700 pixels.

To generate a set of panoramic images that cover all $4\pi$ steradians around the vehicle, synchronous images from the "port" and "starboard" panoramic cameras were first fused to generate a unified field-of-view video stream (Figure 1). The resulting images remove the vehicle from the panoramic images, although the area beneath the cameras remains occluded.

The Ladybug3 cameras are located in front of the detector array in the RadMAP vehicle. To account for this, the time range for detector events is delayed by the velocity-derived time offset between the gamma-ray and image timestamps.

To determine the gamma-ray time bins corresponding to the image locations, the following calculation was performed. Using the image timestamps, the midpoint timestamps $t_i^{\mathrm{img}}$ between subsequent images were calculated. The vehicle speed $s(t)$ was obtained from RadMAP's Inertial Navigation System (INS), and the corresponding NaI midpoint timestamps $t_i^{\mathrm{nai}}$ were calculated by numerically integrating $s(t)$ to satisfy

$$\Delta x = \int_{t_i^{\mathrm{img}}}^{t_i^{\mathrm{nai}}} s(t)dt \tag{8}$$

where $\Delta x = 4.5$ m is the horizontal distance between the NaI array and the cameras. Since the typical vehicle speed during the dataset was $2 - 8$ m/s,

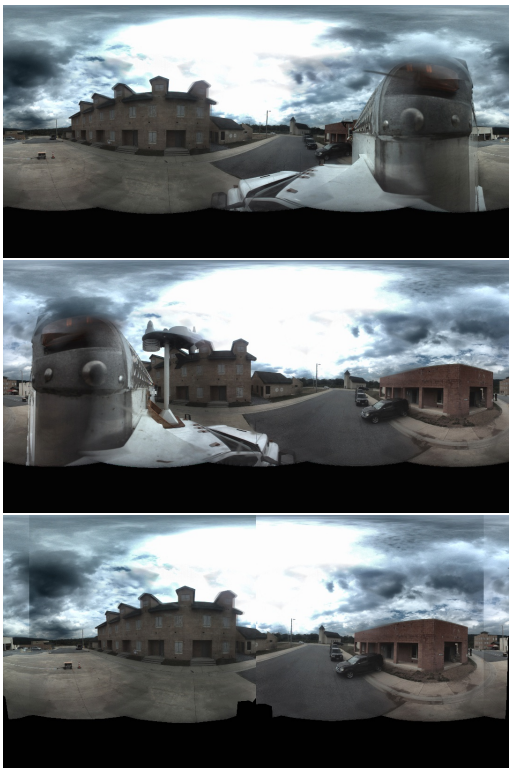

Figure 1: Example of the fusion of a port side panoramic image (top) with a starboard side image (middle) to create a combined panoramic image (bottom) that eliminates most of the occlusion due to the vehicle. (Color online.)

the typical delay between the image timestamps and the NaI timestamps is $0.5 - 2.5$ s, and changes in speed result in slight variations in gamma-ray time bin intervals.

The NaI(Tl) array's timestamps $t_i^{\mathrm{nai}}$ were then used as time boundaries to calculate binned energy spectra. For simplicity, the individual spectra of the 100 NaI(Tl) detectors of RadMAP's 1 $\mathrm{m}^2$ array were summed together into one spectrum, making the array essentially one large monolithic NaI(Tl) detector. The set of spectra will be denoted $\mathbf{x_i}$, and the dwell times $\Delta t_i$. In the end, one spectrum for each image in the set was created, with dwell times ranging from $\approx 0.25 - 0.45$ s.

### *2.3. Image classification*

Each frame in the fused video stream was subjected to an automated segmentation algorithm, Simple Linear Iterative Clustering (SLIC) [12], producing 12,000 "superpixels" for each image. From each superpixel, a 111-dimensional feature vector consisting of the following features was extracted:

- Minimum, mean, and maximum of:
  - Tangent of elevation angle when object is directly to the side: $\tan\theta_{side} = \tan\theta/|\sin\phi|$, where $\theta, \phi$ are the elevation and azimuth angles
- Mean and standard deviation of:
  - RGB colors R, G, and B
  - Lab colors L, a, and b
- Histograms of colors (0–255, 16 bins) for:
  - RGB colors R, G, and B
  - Lab colors L, a, and b

A subset of 46 images were manually labeled with eleven classes: grass, forest, building rooftop, concrete, asphalt, gravel, sky, vehicles, and red, brown, and gray buildings. Each image was then segmented using SLIC, and the superpixels that were completely labeled by exactly one class were then used to train a random forest classifier, which was then applied to all of the images. One-third of the ground truth superpixels were randomly withheld from training and used to generate a confusion matrix for the classifier. Figure 2 shows the normalized confusion matrix, which reveals that most of the classes are found with $> 85\%$ accuracy, however some of the rare classes (building roof, white building, and vehicles) are confused often with more common classes. Further work could be done to improve the classifications through improving the feature vector used or using a more advanced technique such as a neural network, although unsupervised methods would be more broadly applicable and these could additionally

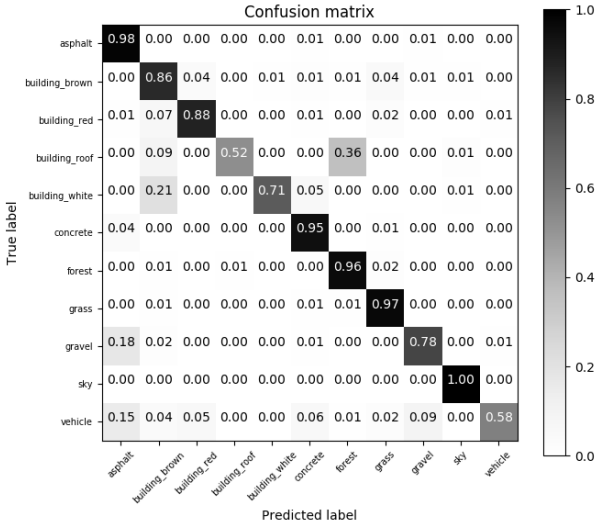


Figure 2: Confusion matrix for the eleven classes classified by the random forest described in the text.

draw from other sources of information such as RadMAP's hyperspectral- and LiDAR-derived clusters and objects.

To fill in the occluded foreground of the images, nearby images were used to infer the unknown region in the following way. The position and heading given by RadMAP's INS were used to transform images within $\pm 5$ s of a given image into the frame of the image assuming that the camera is 3.1 m above an infinite plane. Starting with the images closest in time to a given image, images further and further in time are examined until at least two images have the same classification for the unknown pixel or the images being examined are more than 5 s away from the original image. Any remaining unknown pixels are assigned using a flood-fill from nearby pixels.

One last step is applied to smooth out the classified images. Like the previous step, nearby images are transformed into the frame of a given image, but now assuming the vehicle is within a rectangular box of finite size in order to account for the unknown distance to each pixel. A box of dimensions 10 m to each side, 50 m to front and back, and 3.1 m to the ground yielded qualitatively acceptable

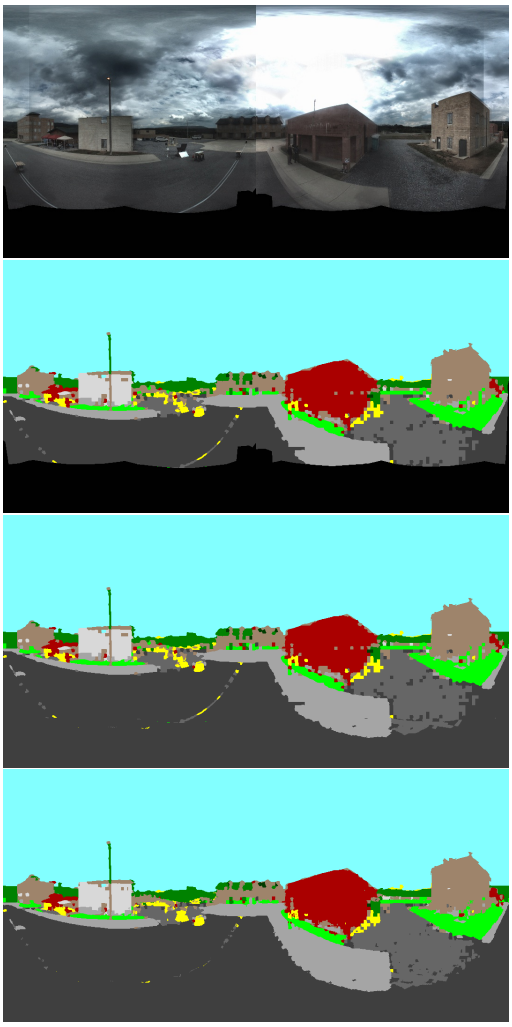

Figure 3: Example of processing a single panoramic image. The original image (top) is divided into superpixels and classified (second). The third image shows the result of using nearby images to fill in the obscured region beneath the cameras, and the last image is the result of using nearby images to smooth out noisy pixels. (Color online.)

results. The image plus the four images closest in time are examined to find the areas where four out of the five images agree on the classification. For the pixels where no four images agree, the original classification is retained.

The results of these image classification and processing steps for a single image are shown in Figure 3.

### 2.4. Detector effective area

The effective area $A_{ij}$ was calculated using Monte Carlo simulations of the RadMAP vehicle. A mass model of the entire vehicle and its detector systems was developed in MEGAlib [13] (see Figure 4). To obtain the measured spectrum for each of the NaI(Tl) detectors from gamma rays originating from any point in $4\pi$ steradians, monoenergetic point sources were simulated at 520 points subtending the unit sphere, and the results were interpolated. The points were at a distance of 10 m from the NaI(Tl) array center so as to be in the far field. All simulations were performed in a vacuum. The energies chosen were major background and source lines: 238, 295, 351, 583, 609, 662, 911, 968, 1112, 1460, 1764, 2200, and 2615 keV. Since the spectral features examined in Section 3 are summed counts in a spectrum, the effective area was determined by summing over the entirety of the simulated energy deposition spectra. Figure 5 shows the effective area derived from these simulations for incident 1460 keV photons that deposit any energy in the detectors.

To determine the effective area for a non-monoenergetic source $A_S$, a simple estimation was performed in the following fashion. Let $S(E)$ be the measured spectrum of the source whose effective area we want to estimate, and let $E_j$ be the set of energies that were simulated. Then the effective area for $S(E)$ was estimated using a weighted average of the monoenergetic effective areas:

$$A_S \approx \frac{\sum_j A(E_j)S(E_j)}{\sum_j S(E_j)} \tag{9}$$

where we have implicitly assumed that the incident spectrum is similar to the measured spectrum $S$ and that the discrete set of energies $E_j$ sufficiently spans the energy space. Then $A_S$ is an approximation to the effective area for an incident photon from a spectrum $S$ to interact in the detector array.

### 2.5. Solid angle

The solid angle $\Delta\Omega_{ij}$ was calculated using the projection of the panoramic images. In this case, the projection was equal in angles, so each pixel of the

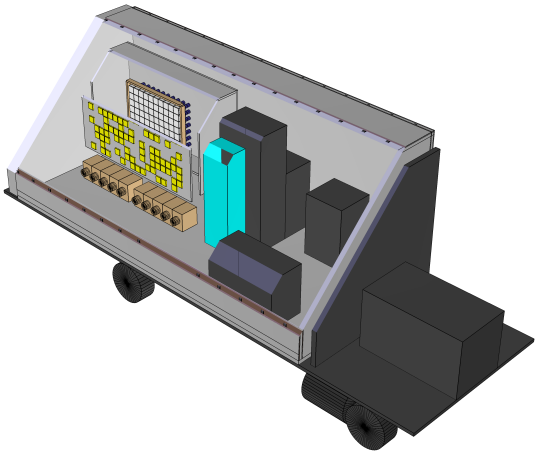

Figure 4: Cutaway visualization of the MEGAlib mass model used for the RadMAP vehicle showing the NaI(Tl) array (white) toward the rear of the vehicle behind a coded mask (lead mask elements are yellow). View is from the front starboard side of the vehicle. (Color online.)

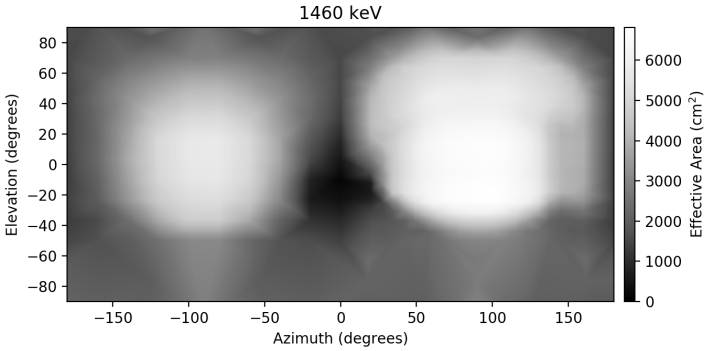


Figure 5: Simulated effective area (product of geometric area and detector efficiency) for the RadMAP NaI(Tl) array calculated for monoenergetic 1460 keV photons that deposit any energy in the detectors. The elevation angle is $\theta$ and azimuth is $\phi$. The projection of this image is made to directly correspond to the visual panoramic images, so $(\theta, \phi) = (0°, 90°)$ points directly out the right (starboard) side of the vehicle and is also the center of the NaI(Tl) coded mask field of view, while $(\theta, \phi) = (0°, -90°)$ points directly out the left (port) side of the vehicle.

image had the same width in elevation and azimuth. The solid angle of a pixel

at elevation angle $\theta$ and azimuth $\phi$ is therefore

$$\Delta\Omega = \cos\theta\,\Delta\theta\,\Delta\phi \tag{10}$$

where $\Delta\theta$ and $\Delta\phi$ are the height and width of each pixel in radians.

However, because the panoramic cameras are located at a significantly higher elevation than center of the detector system (3.12 m versus 2.29 m), $\Delta\Omega$ will be distorted. This distortion will be especially pronounced for nearby pixels, particularly those on the ground near the vehicle. Note that no significant overhanging features exist at the FTIG facility. To correct for the decreased distance to points on the ground, solid angles with $\theta < 0$ are multiplied by the factor

$$\frac{\Delta\Omega'}{\Delta\Omega} = \frac{z^2}{\sin^2\theta + z^2\cos^2\theta} \tag{11}$$

where $z$ is the ratio of the camera height to the center of the NaI(Tl) array, or 1.37. This factor accounts only for changes in distance, not changes to the surface normals, although for a full correction the surface normal would need to be known.

### *2.6. Image response*

Finally, with $4\pi$ panoramic images labeled according to material class, NaI(Tl) spectra collocated with the images, spectrum dwell times $\Delta t$ calculated, effective area $A_S$ estimated from simulations, and solid angle $\Delta\Omega$ calculated from the image projection, we can calculate the response matrices $R$ using Equation (7) and fit the linear emission model (Equation (6)). Figure 6 shows the responses $R$ at 1460 keV for the different material classes derived from a subset of the image dataset that comprised one "figure eight" of the MOUT facility. In the following section, the responses for the entire dataset will be fit to different spectral features.

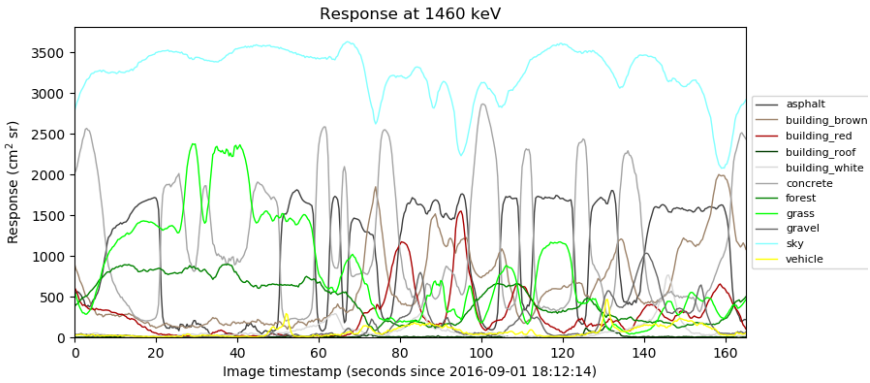


Figure 6: Responses for each image class for monoenergetic photons at 1460 keV. The data shown are a subset of the total data set, a 165 s long "figure eight" around the FTIG MOUT facility. (Color online.)

## 3. Correlation analyses

With the image-derived responses and gamma-ray spectra in hand, we now turn to the problem of finding correlations and comparing the results with the ground truth.

### *3.1. Gross counts*

The simplest feature to examine in the gamma-ray data is the gross count rate, which is plotted as the colorization of the mobile system path for a portion of the dataset in Figure 7. The figure shows that the gross count rate is highest away from the buildings and lowest along the central street.

The responses for each material class were fit using maximum likelihood expectation maximization (MLEM) to the gross counts according to Equation (6). Fit results are shown in Figure 8, and comparisons to ground truth measurements are shown in Table 1.

### *3.2. Non-negative matrix factorization*

In order to fit the full spectrum instead of only gross counts, non-negative matrix factorization (NMF) [14, 15] was employed as a spectral dimensionality-reduction technique. Though well known in other fields of study, NMF has

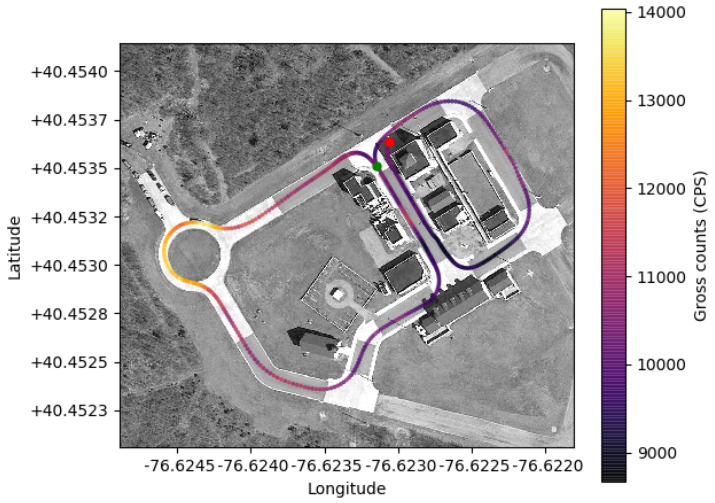


Figure 7: The gross count rate for the "figure eight" loop around the FTIG MOUT facility shown in Figure 6. The vehicle track begins at the green point and ends at the red point. Color online. (Map imagery: Google.)

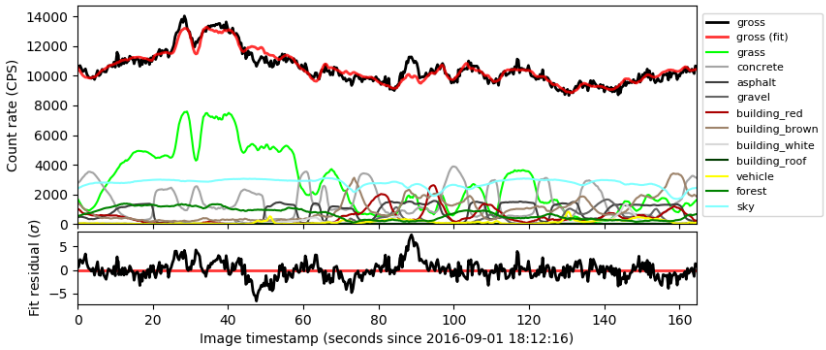


Figure 8: A linear combination of image class responses fit to the gross counts for the summed NaI(Tl) array. The grass/soil class is the dominant contributor, followed by the sky. Data shown are for the 165 s "figure eight" loop around the FTIG MOUT facility shown in Figures 6 and 7, and the fit was performed only on the subset of data shown. (Color online.)

only recently been applied to gamma-ray spectroscopic data [16]. NMF seeks a decomposition of a matrix of non-negative data $\mathbf{X}$ into non-negative matrices

of coefficients $\mathbf{A}$ and components $\mathbf{V}$, i.e.,

$$\mathbf{X} \approx \mathbf{A} \cdot \mathbf{V}, \tag{12}$$

that minimizes the Poisson negative log likelihood of $\mathbf{X}$ given $\hat{\mathbf{X}} \equiv \mathbf{A} \cdot \mathbf{V}$, i.e.,

$$\Lambda(\mathbf{X}|\hat{\mathbf{X}}) = \sum \left( \hat{\mathbf{X}} - \mathbf{X} \odot \log(\hat{\mathbf{X}}) \right), \tag{13}$$

where multiplication ($\odot$) and log are applied elementwise. For this analysis, $\mathbf{X}$ is a matrix where each row is a measured spectrum $\mathbf{x_i}$. For example, a two-component NMF decomposition has the form:

$$\begin{bmatrix} \mathbf{x_0}^T \\ \mathbf{x_1}^T \\ \mathbf{x_2}^T \\ \vdots \end{bmatrix} \approx \begin{bmatrix} a_{00} & a_{01} \\ a_{10} & a_{11} \\ a_{20} & a_{21} \\ \vdots & \vdots \end{bmatrix} \cdot \begin{bmatrix} \mathbf{v_0}^T \\ \mathbf{v_1}^T \end{bmatrix} \tag{14}$$

where $\mathbf{v_0}$ and $\mathbf{v_1}$ are the two spectral components that describe the data. Therefore, each spectrum can be expressed as a linear sum of the two components:

$$\mathbf{x_i} \approx \hat{\mathbf{x}}_\mathbf{i} = a_{i0}\mathbf{v_0} + a_{i1}\mathbf{v_1} \tag{15}$$

where $\hat{\mathbf{x}}_\mathbf{i}$ is the NMF fit to the spectrum $\mathbf{x_i}$.

NMF was chosen for dimensionality reduction over other methods due to its non-negativity, consistency with Poisson statistics, and linearity — all of these properties allow the model to represent the underlying photon source emissions in a valid manner. The dimensionality reduction methods Principal Component Analysis (PCA) and Singular Value Decomposition (SVD) are similar but are disfavored because their weights and components can be negative, and they assume Gaussian statistics. In addition, Poisson Principal Component Analysis (PPCA) [17] was not used because although PPCA is non-negative and abides by Poisson statistics, the decomposition is neither linear nor additive, but is

instead multiplicative. One drawback to using NMF over other methods is that the number of components must be chosen before calculating the decomposition. Although the NMF model is consistent with radiation physics, like all dimensionality-reduction methods, it is not guaranteed to represent the true photon emission spectra.

The one-component NMF decomposition is nearly identical to gross counts since the single component will approximate (normalized) mean spectrum and the weight will approximate the gross counts in the spectrum. Therefore the one-component NMF analysis is essentially the same as the gross count analysis in Section 3.1. Instead, we will examine the results from a two-component NMF model.

The two-component NMF solution yields two spectral components with different spectral features (Figure 9). The first component can be interpreted as being due to distant and skyshine sources because of the lack of strong line features and the high continuum present near 100 keV, presumably due to multiple scatters in the environment. Component 2 may result from nearby sources due to several line features and a higher low energy rollover. These interpretations are supported by the component weights when displayed on a map — component 1 is dominant in open areas away from the buildings, while component 2 is strongest in the areas near buildings and when surrounded by soil (Figure 10).

For simplicity, the component weights for components 1 and 2 were fit separately to the data using weighted non-negative least squares to solve Equation (6). The weights used were the inverse of the standard errors for the component weights, which were derived from $\Lambda$. The resulting fits are shown in Figure 11.

### *3.3. Comparison with ground truth*

Table 1 shows the ground truth activities determined using *in situ* HPGe measurements [11] compared to fits to gross counts and NMF components from RadMAP. Overall, the activities derived from gross counts are similar in magnitude to the ground truth, and the soil/grass class has the largest activity.

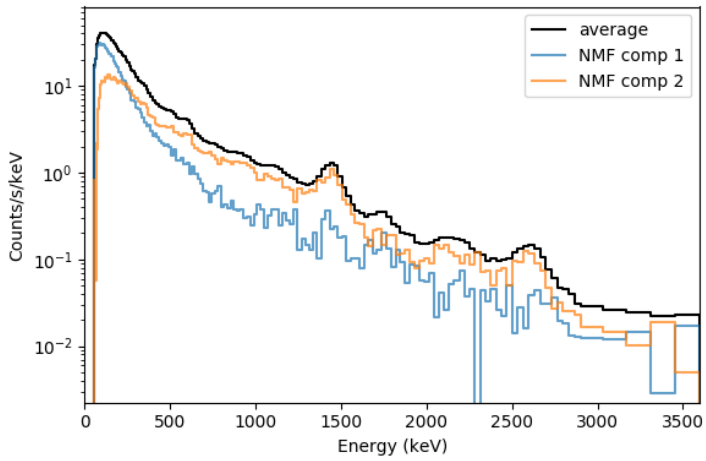


Figure 9: The two NMF components found using maximum likelihood to fit the spectra in the FTIG MOUT dataset. (Color online.)

However, nearly all of the activities are significantly higher than the ground truth values, but this discrepancy may be due to the fact that the ground truth analysis isolated the foreground material from any materials behind it, which also would contribute to the photon flux passing out of the surface.

Another feature of the results is that in general the two NMF component activities all approximately sum to the gross counts activity, so it is illustrative to compare how the class activities are apportioned between the two components. The soil/grass activity gets nearly evenly split between both components, indicating that it is a significant contributor both to nearby and distant sources. The building material types are apportioned more heavily to component 2, which is consistent with that component representing nearby sources. Likewise forest and sky are more heavily apportioned to component 1, and these classes are clear markers that the detectors are in open areas and thus more sensitive to distant sources.

Table 2 shows the same fit results as Table 1 but from a fit of only 165 s of data from the single "figure eight" lap of the facility, which was shown in Figures 6, 7, 8, 10, and 11. In comparison to Table 1, significantly less flux is

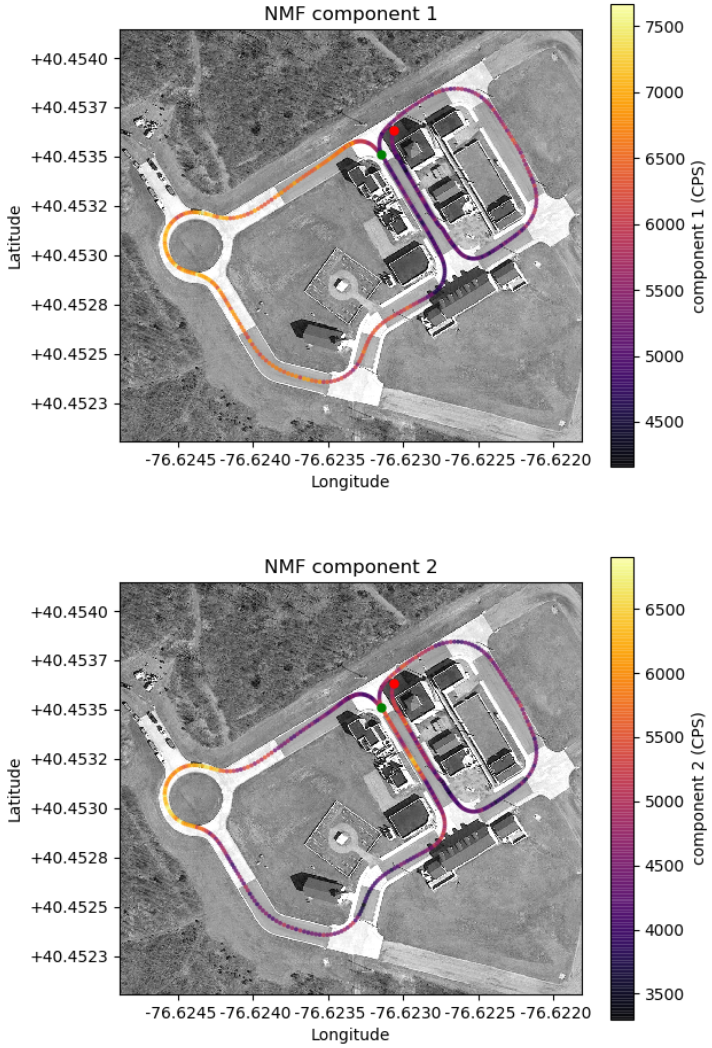


Figure 10: The two NMF component weights for the "figure eight" loop around the FTIG MOUT facility shown in Figures 6, 7, and 8. Color online. (Map imagery: Google.)

attributed to the sky and the forest, while more flux is attributed to vehicles, especially for NMF component 2.

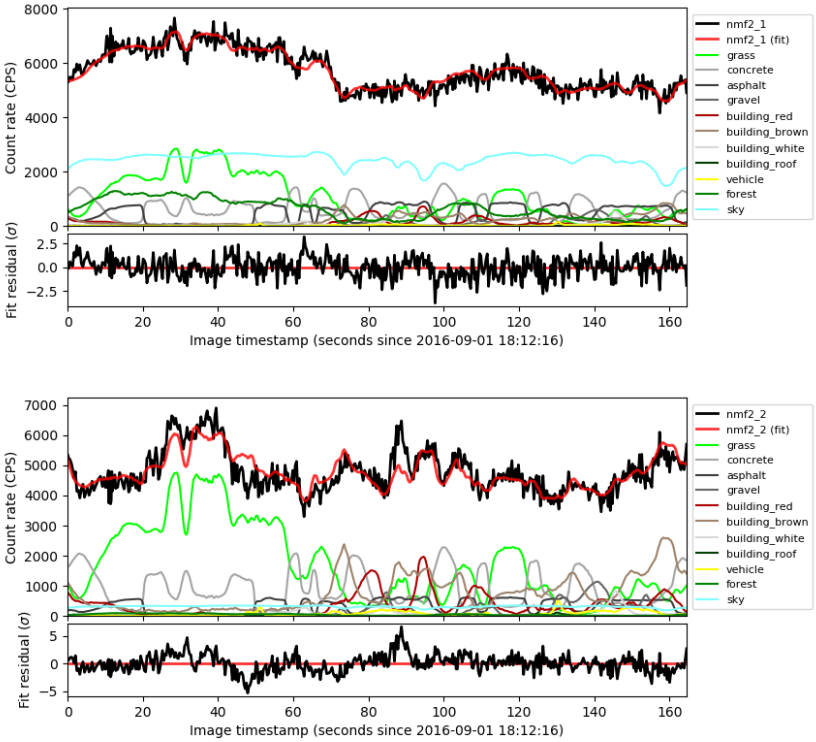


Figure 11: A linear combination of image class responses fit to the two NMF components for the 165 s "figure eight" loop around the FTIG MOUT facility shown in Figures 6, 7, 8, and 10. The fit was performed only on the subset of data shown. (Color online.)

## 4. Discussion

The analysis of RadMAP data has shown that it is possible to use the presented radiological background inversion method to achieve a semi-quantitative understanding of the radiological gamma-ray source terms of an environment around a detector system. This method leveraged a thoroughly understood angle-dependent detector response model and assumed the environment can be divided up into a small number of radiologically distinct materials. This result gives hope that results of similar quality could be obtained from analyses of data collected in urban environments. Such a method of determining the gamma-emitting characteristics of benign materials found in urban settings can

| Class | Ground truth (phot/s/cm$^2$) | Gross counts | NMF comp. 1 | NMF comp. 2 |
|---|---|---|---|---|
| soil/grass | 2.462 | $3.629 \pm 0.017$ | $1.660 \pm 0.025$ | $1.936 \pm 0.023$ |
| concrete | 0.985 | $1.291 \pm 0.018$ | $0.694 \pm 0.026$ | $0.537 \pm 0.024$ |
| asphalt | 0.836 | $0.871 \pm 0.019$ | $0.654 \pm 0.029$ | $0.160 \pm 0.027$ |
| gravel | 0.831 | $1.545 \pm 0.021$ | $0.804 \pm 0.030$ | $0.726 \pm 0.028$ |
| red building | 0.397 | $2.050 \pm 0.007$ | $0.717 \pm 0.009$ | $1.352 \pm 0.009$ |
| dark tan building | 0.446 | $2.354 \pm 0.008$ | $0.720 \pm 0.012$ | $1.660 \pm 0.011$ |
| light tan building | 0.658 | $\star$ | $\star$ | $\star$ |
| white building | 0.311 | $1.632 \pm 0.022$ | $0.750 \pm 0.032$ | $0.905 \pm 0.031$ |
| gray building | 0.501 | $\star$ | $\star$ | $\star$ |
| building roof | N/A | $0.000 \pm 0.084$ | $0.000 \pm 0.144$ | $0.000 \pm 0.134$ |
| vehicle | N/A | $0.870 \pm 0.038$ | $0.144 \pm 0.056$ | $0.609 \pm 0.052$ |
| forest | N/A | $2.684 \pm 0.021$ | $1.828 \pm 0.031$ | $0.960 \pm 0.029$ |
| sky | N/A | $1.537 \pm 0.012$ | $1.047 \pm 0.017$ | $0.550 \pm 0.016$ |

Table 1: Comparison of ground truth surface fluxes with fits to the spectral features described in the text. Units are photons/s/cm$^2$ and errors are statistical. The $\star$ symbol indicates that the "dark tan" and "light tan" classes and the "white" and "gray" classes were separate in the HPGe ground truth measurements but were combined for the RadMAP analysis.

| Class | Ground truth (phot/s/cm$^2$) | Gross counts | NMF comp. 1 | NMF comp. 2 |
|---|---|---|---|---|
| soil/grass | 2.462 | $4.50 \pm 0.10$ | $1.77 \pm 0.15$ | $2.74 \pm 0.14$ |
| concrete | 0.985 | $2.09 \pm 0.09$ | $0.90 \pm 0.14$ | $1.18 \pm 0.13$ |
| asphalt | 0.836 | $1.43 \pm 0.10$ | $0.88 \pm 0.15$ | $0.56 \pm 0.14$ |
| gravel | 0.831 | $2.15 \pm 0.11$ | $0.81 \pm 0.16$ | $1.44 \pm 0.14$ |
| red building | 0.397 | $2.36 \pm 0.05$ | $0.69 \pm 0.07$ | $1.72 \pm 0.06$ |
| dark tan building | 0.446 | $2.03 \pm 0.05$ | $0.52 \pm 0.06$ | $1.52 \pm 0.06$ |
| light tan building | 0.658 | $\star$ | $\star$ | $\star$ |
| white building | 0.311 | $2.00 \pm 0.10$ | $0.82 \pm 0.14$ | $1.23 \pm 0.14$ |
| gray building | 0.501 | $\star$ | $\star$ | $\star$ |
| building roof | N/A | $0.00 \pm 0.61$ | $0.00 \pm 0.89$ | $1.09 \pm 0.83$ |
| vehicle | N/A | $2.59 \pm 0.28$ | $0.49 \pm 0.41$ | $1.55 \pm 0.37$ |
| forest | N/A | $1.86 \pm 0.10$ | $1.78 \pm 0.14$ | $0.13 \pm 0.14$ |
| sky | N/A | $1.08 \pm 0.06$ | $0.98 \pm 0.09$ | $0.12 \pm 0.09$ |

Table 2: Comparison of ground truth surface fluxes with fits to only the 165 s "figure eight" subset shown in Figures 8 and 11. Units are photons/s/cm$^2$ and errors are statistical.

facilitate a broader understanding of both observed and expected radiological measurements in mobile radiological search scenarios. This method has the potential to revolutionize the way that such searches are planned and performed, and to enable search algorithms to leverage additional sources of information. However there are caveats to this conclusion.

The first caveat is that the ground truth measurements have revealed that

the FTIG MOUT facility does not have a large degree of variability in potassium, uranium, and thorium levels [11]. In addition, the site was cleared and constructed out of relatively uniform materials within a relatively short amount of time, which is not going to be true of many urban scenes in the world. So it is likely that the MOUT facility is an unusually simple case for background inversion.

The second caveat is that one cannot know *a priori* how many material classifications are needed, nor whether a particular class is even radiologically uniform. Having a small, consistent site like the MOUT facility avoids this problem for now but it will be a major hurdle when analyzing other urban scenes. New developments in semantic segmentation may help with the problem of discovering a reasonable number of material classes, but the radiological uniformity of those classes will always be unknown.

The third caveat is that even if the model is the correct representation of the radiological environment, the inversion solution will always be affected by the measurement uncertainties. With infinitesimally small uncertainties, the background inversion solution would be exact so long as the rank of $R$ is at least the number of material classes. The matrix $R$ could be rank deficient either from having fewer images than material classes, or having at least one column be a linear combination of the other columns. The first problem is avoided by analyzing a sufficient amount of data, and the second problem becomes less likely as the environment becomes more complex. Assuming $R$ is not rank deficient, the measurement uncertainties would be responsible for systematic errors and for high variances on the activities derived for classes with relatively small responses (e.g., the building roof and vehicle classes).

Despite these caveats, there are still many reasons to pursue background inversion and more areas to explore. One reason is that there is much more information in the RadMAP radiological data to be exploited than was explored in this work. For example, the NaI(Tl) array on RadMAP was built as a coded mask imager, but here it was considered as a single large detector. Further data analysis separately treating each detector, its position, and its calculated

response could make the inversion analysis both more sensitive to the spatial distribution of background gamma-ray emissions and less subject to errors in the near field. Indeed, an entire array of HPGe detectors was neglected in this work but could also be utilized in future analyses.

Another area to explore is the robustness of inversion, which could be examined by fitting different subsets of the larger dataset. Already this work has shown the difference between the analysis of the hour-long dataset (Table 1) and the analysis of a 165 s "figure eight" subset of the dataset (Table 2). Although the vehicle drove around the entire MOUT facility in the "figure eight" subset, it was not a uniform sample of the full dataset since in the full dataset the vehicle traversed each road in both directions over multiple passes. The differences between Table 1 and Table 2 are beyond what could be justified by statistical uncertainties, which gives some indication of how differing perspectives can impact this analysis. Exploring the robustness of this background inversion analysis across subsets of this dataset could better inform the systematic nature of the uncertainties that are observed in the comparison between the tables. For example, the solutions for identical laps at the MOUT facility could be compared to each other to examine the repeatability of inversion over multiple nearly identical measurements. Another investigation would be to fit only the previous $T$ seconds of data and see how well the fit matches the next few seconds of data, for different values of $T$.

A final reason that background inversion could have promise in the general case is that there is still much more information about the environment than has been analyzed here. This work has examined panoramic visual imagery, but RadMAP also operated two rotating LiDAR units, so three-dimensional models of the environment can be constructed. RadMAP also carried two hyperspectral cameras, so better material classification and identification can be performed than RGB cameras allow. With a three-dimensional model of the environment with better material identification, a much more sophisticated model could be developed and compared with the measurements (e.g., air attenuation and second-order scattering could be considered). Three-dimensional models

also eliminate the need to compensate for the relative positioning of the cameras and detectors, and the need to fill in occluded areas unseen by the cameras, since such information would be intrinsic to the model rather than "patched" later on. Developing a background inversion framework that uses three-dimensional models and leverages individual detectors in the subject of future study.

## Acknowledgment

This work was performed under the auspices of the US Department of Energy by Lawrence Berkeley National Laboratory under Contract DE-AC02-05CH11231. The project was funded by the US Department of Energy, National Nuclear Security Administration, Office of Defense Nuclear Nonproliferation Research and Development (DNN R&D).

## References

[1] K.-P. Ziock, M. Cunningham, L. Fabris, Two-sided coded-aperture imaging without a detector plane, in: IEEE Nuclear Science Symposium Conference Record, 2008. NSS '08, 2008, pp. 634–641. doi:10.1109/NSSMIC.2008.4775216.

[2] E. A. Wulf, B. F. Phlips, W. Neil Johnson, B. Leas, L. J. Mitchell, MISTI imaging and source localization, in: IEEE Nuclear Science Symposium Conference Record, 2008. NSS '08, 2008, pp. 2413–2417. doi:10.1109/NSSMIC.2008.4774842.

[3] R. D. Penny, W. E. Hood, R. M. Polichar, F. H. Cardone, L. G. Chavez, S. G. Grubbs, B. P. Huntley, R. A. Kuharski, R. T. Shyffer, L. Fabris, K. P. Ziock, S. E. Labov, K. Nelson, A dual-sided coded-aperture radiation detection system, Nuclear Instruments and Methods in Physics Research Section A: Accelerators, Spectrometers, Detectors and Associated Equipment 652 (1) (2011) 578–581. doi:10.1016/j.nima.2011.01.161.

URL http://www.sciencedirect.com/science/article/pii/S0168900211002634

[4] K.-P. Ziock, K. E. Nelson, Maximum detector sizes required for orphan source detection, Nuclear Instruments and Methods in Physics Research Section A: Accelerators, Spectrometers, Detectors and Associated Equipment 579 (1) (2007) 357–362. doi:10.1016/j.nima.2007.04.061.
URL http://www.sciencedirect.com/science/article/pii/S016890020700647X

[5] T. Aucott, M. Bandstra, V. Negut, J. Curtis, D. Chivers, K. Vetter, Effects of Background on Gamma-Ray Detection for Mobile Spectroscopy and Imaging Systems, IEEE Transactions on Nuclear Science 61 (2) (2014) 985–991. doi:10.1109/TNS.2014.2306998.

[6] R. D. Penny, T. M. Crowley, B. M. Gardner, M. J. Mandell, Y. Guo, E. B. Haas, D. J. Knize, R. A. Kuharski, D. Ranta, R. Shyffer, S. Labov, K. Nelson, B. Seilhan, J. D. Valentine, Improved radiological/nuclear source localization in variable NORM background: An MLEM approach with segmentation data, Nuclear Instruments and Methods in Physics Research Section A: Accelerators, Spectrometers, Detectors and Associated Equipment 784 (Supplement C) (2015) 319–325. doi:10.1016/j.nima.2015.01.025.
URL http://www.sciencedirect.com/science/article/pii/S0168900215000522

[7] T. H. Joshi, R. J. Cooper, J. Curtis, M. Bandstra, B. R. Cosofret, K. Shokhirev, D. Konno, A Comparison of the Detection Sensitivity of the Poisson Clutter Split and Region of Interest Algorithms on the RadMAP Mobile System, IEEE Transactions on Nuclear Science 63 (2) (2016) 1218–1226. doi:10.1109/TNS.2016.2537206.

[8] M. S. Bandstra, T. J. Aucott, E. Brubaker, D. H. Chivers, R. J. Cooper, J. C. Curtis, J. R. Davis, T. H. Joshi, J. Kua, R. Meyer, V. Negut,

M. Quinlan, B. J. Quiter, S. Srinivasan, A. Zakhor, R. Zhang, K. Vetter, RadMAP: The Radiological Multi-sensor Analysis Platform, Nuclear Instruments and Methods in Physics Research Section A: Accelerators, Spectrometers, Detectors and Associated Equipment 840 (2016) 59–68. doi:10.1016/j.nima.2016.09.040.
URL http://www.sciencedirect.com/science/article/pii/S0168900216309780

[9] A. D. Nicholson, I. Garishvili, D. E. Peplow, D. E. Archer, W. R. Ray, M. W. Swinney, M. J. Willis, G. G. Davidson, S. L. Cleveland, B. W. Patton, D. E. Hornback, J. J. Peltz, M. S. L. McLean, A. A. Plionis, B. J. Quiter, M. S. Bandstra, Multiagency Urban Search Experiment Detector and Algorithm Test Bed, IEEE Transactions on Nuclear Science 64 (7) (2017) 1689–1695. doi:10.1109/TNS.2017.2677092.

[10] D. E. O. Archer, M. S. Bandstra, G. G. O. Davidson, S. L. Cleveland, I. O. Garishvili, D. E. Hornback, J. O. Johnson, M. S. L. McLean, A. D. O. Nicholson, B. W. O. Patton, D. E. O. Peplow, A. A. Plionis, B. J. Quiter, W. R. O. Ray, A. J. Rowe, M. W. O. Swinney, M. J. O. Willis, Modeling Urban Scenarios & Experiments: Fort Indiantown Gap Data Collections Summary and Analysis, Tech. Rep. ORNL/LTR-2017/371, Oak Ridge National Lab. (ORNL), Oak Ridge, TN (United States) (Oct. 2017). doi:10.2172/1410932.
URL https://www.osti.gov/biblio/1410932

[11] M. W. Swinney, D. E. Peplow, B. W. Patton, A. D. Nicholson, D. E. Archer, M. J. Willis, A Methodology for Determining the Concentration of Naturally Occurring Radioactive Materials in an Urban Environment, Nuclear Technology 0 (0) (2018) 1–11. doi:10.1080/00295450.2018.1458558.
URL https://doi.org/10.1080/00295450.2018.1458558

[12] R. Achanta, A. Shaji, K. Smith, A. Lucchi, P. Fua, S. Süsstrunk, SLIC Superpixels Compared to State-of-the-Art Superpixel Methods, IEEE Trans-

actions on Pattern Analysis and Machine Intelligence 34 (11) (2012) 2274–2282. doi:10.1109/TPAMI.2012.120.

[13] A. Zoglauer, R. Andritschke, F. Schopper, MEGAlib – The Medium Energy Gamma-ray Astronomy Library, New Astronomy Reviews 50 (7) (2006) 629–632. doi:10.1016/j.newar.2006.06.049.
URL http://www.sciencedirect.com/science/article/pii/S1387647306000972

[14] P. Paatero, U. Tapper, Positive matrix factorization: A non-negative factor model with optimal utilization of error estimates of data values, Environmetrics 5 (2) (1994) 111–126. doi:10.1002/env.3170050203.
URL https://onlinelibrary.wiley.com/doi/abs/10.1002/env.3170050203

[15] D. D. Lee, H. S. Seung, Learning the parts of objects by non-negative matrix factorization, Nature 401 (6755) (1999) 788–791. doi:10.1038/44565.
URL http://www.nature.com/nature/journal/v401/n6755/abs/401788a0.html

[16] K. J. Bilton, T. H. Joshi, M. S. Bandstra, J. C. Curtis, B. J. Quiter, R. J. Cooper, K. Vetter, Gamma-Ray Background Modeling, Detection, and Identification using Non-negative Matrix Factorization (submitted to IEEE Transactions on Nuclear Science).

[17] P. Tandon, Bayesian Aggregation of Evidence for Detection and Characterization of Patterns in Multiple Noisy Observations, Ph.D., Carnegie Mellon University, United States – Pennsylvania (2015).
URL https://search.proquest.com/docview/1774007802/abstract/463397BF9CAF4561PQ/1